



## Full length article

## Discovery of Guinier-Preston zone hardening in refractory nitride ceramics

O.V. Pshyk<sup>a,1,\*</sup>, X. Li<sup>a</sup>, I. Petrov<sup>a,b</sup>, D.G. Sangiovanni<sup>a</sup>, J. Palisaitis<sup>a</sup>, L. Hultman<sup>a</sup>, G. Greczynski<sup>a</sup>

<sup>a</sup> Thin Film Physics Division, Department of Physics, Chemistry and Biology (IFM), Linköping University, Linköping SE-581 83, Sweden

<sup>b</sup> Materials Research Laboratory, University of Illinois, Urbana, IL 61801, United States

## ARTICLE INFO

## Keywords:

Guinier-Preston zone  
TiAlN  
Ceramics  
Age hardening  
Spinodal decomposition

## ABSTRACT

Traditional age hardening mechanisms in refractory ceramics consist of precipitation of fine particles. These processes are vital for widespread wear-resistant coating applications. Here, we report novel Guinier-Preston zone hardening, previously only known to operate in soft light-metal alloys, taking place in refractory ceramics like multicomponent nitrides. The added superhardening, discovered in thin films of Ti-Al-W-N upon high temperature annealing, comes from the formation of atomic-plane-thick W disks populating {111} planes of the cubic matrix, as observed by atomically resolved high resolution scanning transmission electron microscopy and corroborated by *ab initio* calculations and molecular dynamics simulations. Guinier-Preston zone hardening concurrent with spinodal decomposition is projected to exist in a range of other ceramic solid solutions and thus provides a new approach for the development of advanced materials with outstanding mechanical properties and higher operational temperature range for the future demanding applications.

## 1. Introduction

TiAlN-based compounds are subject to intense research as wear-protective coatings and films for surfaces exposed to extreme conditions such as high working temperature and severe friction [1–3]. The crucial role of Al, apart from increasing film hardness, is to enhance the thermal stability and oxidation resistance during operation at elevated temperature [4,5]. The Al solubility in B1-NaCl-type TiN (*c*-TiN) is, however, expected to be < 20 at.% under equilibrium conditions at 1300 °C [6]. Yet, supersaturated metastable single phase cubic *c*-Ti<sub>1-x</sub>Al<sub>x</sub>N films with desired extended Al solubility on the metal sublattice  $x = \text{Al}/(\text{Al}+\text{Ti})$  can be synthesized under non-equilibrium growth conditions by physical vapor deposition (PVD) techniques such as direct current magnetron sputtering (DCMS) [7], cathodic arc deposition [8], and high-power impulse magnetron sputtering (HiPIMS) [9]. The maximum  $x$  in *c*-Ti<sub>1-x</sub>Al<sub>x</sub>N film reaches ~ 0.55 with DCMS [10], 0.64 with hybrid HiPIMS/DCMS [11], and 0.66 with cathodic arc evaporation [12], respectively.

The thermodynamic miscibility gap in the *c*-Ti<sub>1-x</sub>Al<sub>x</sub>N system is in the range  $0.3 \leq x \leq 1$  at temperatures around ~1000 °C [6]. The driving force towards decomposition increases with  $x$  and reaches a maximum at  $x \approx 0.7$ . At elevated temperatures (~900–1000 °C), supersaturated

metastable *c*-Ti<sub>1-x</sub>Al<sub>x</sub>N undergoes isostructural decomposition into coherent *c*-AlN-rich and *c*-TiN-rich nanodomains via spinodal mechanism [13].

The coherency strain between TiN-rich and AlN-rich domains caused by the decomposition of the original phase hinders the movement of dislocations and promotes age hardening [13,14]. Subsequent over-aging, achieved either by annealing at even higher temperatures (~ 950–1100 °C) or for a longer time, leads to the transformation of cubic AlN-rich domains into thermodynamically stable hexagonal wurtzite-structured (B4) AlN phase (*h*-AlN) through nucleation and growth [15]. As a consequence of relieving coherency strains and the presence of softer *h*-AlN, the hardness significantly decreases [16].

Alloying Ti-Al-N with group IVb and Vb transition metals (such as Zr, Hf, and Nb [17–19]) has shown to be an efficient way for postponing *h*-AlN formation to higher annealing temperatures, but shifting the onset of the spinodal decomposition process together with related age-hardening to lower annealing temperatures. Although alloying with Mo allows to postpone precipitation of *h*-AlN to higher temperatures, age-hardening from spinodal decomposition only partially counteracted the hardness decrease due to second-phase precipitation, recovery processes and grain coarsening [20]. Alloying with Ta retards *h*-AlN formation and shifts age-hardening from spinodal decomposition

\* Corresponding author.

E-mail address: [oleksandr.pshyk@liu.se](mailto:oleksandr.pshyk@liu.se) (O.V. Pshyk).

<sup>1</sup> Present address: Laboratory for Surface Science and Coating Technologies, Empa – Swiss Federal Laboratories for Materials Science and Technology, Switzerland.

to higher temperatures [21,22]. Alloying Ti-Al-N with W, neighbor to Ta and thus a natural extension for exploration, has been by far less studied. Reeswinkel et al. reported Ti-Al-W-N films deposited by DCMS and HiPIMS with the W fraction varying in a wide range from 0.06 to 0.75 [23]. However, no annealing experiments were conducted on these films. Glatz et al. investigated  $\text{Ti}_{0.54}\text{Al}_{0.44}\text{W}_{0.02}\text{N}$ ,  $\text{Ti}_{0.53}\text{Al}_{0.42}\text{W}_{0.05}\text{N}$ , and  $\text{Ti}_{0.50}\text{Al}_{0.41}\text{W}_{0.09}\text{N}$  films deposited by cathodic arc [24]. Those films contained body-centered cubic W (*bcc*-W) phase in the as-deposited state. Annealing experiments revealed a significant hardness increase of the films with W content of 0.05 in the temperature range up to 1000 °C, which was assigned to the *c*-AlN formation. However, no detailed microscopy evidences were provided.

Here, we report on a novel age hardening mechanism identified in a W-containing TiAlN refractory ceramic. Demonstration is made for  $\text{Ti}_{0.53}\text{Al}_{0.39}\text{W}_{0.08}\text{N}$  films grown by hybrid W-HiPIMS/TiAl-DCMS co-sputtering with metal-ion-synchronized substrate bias and no intentional substrate heating (substrate temperature  $T_s < 140$  °C) [25,26]. Upon 2 h long annealing in vacuum, a continuous increase in the nanoindentation hardness  $H$  is observed up to the maximum annealing temperature ( $T_a$ ) of 1000 °C, despite the fact that the softer *h*-AlN phase is detected already after annealing at  $T_a = 900$  °C. The hardening is ascribed to the formation of atomic-layer-thick W disks populating {111} planes of the cubic matrix, known from light-metal alloys as Guinier-Preston (GP) zones [27]. Interestingly, in films with higher AlN content,  $\text{Ti}_{0.33}\text{Al}_{0.62}\text{W}_{0.05}\text{N}$ , W ordering does not take place due to the onset of the cubic matrix decomposition and precipitation of *h*-AlN at a lower temperature. Instead, *bcc*-W phase is detected after 2 h at 900 °C and film hardness follows classical evolution upon annealing, first an increase in  $H$  due to *c*-AlN formation followed by a rapid drop once the *h*-AlN (and *bcc*-W) precipitates. The occurrence of the new hardening mechanism related to GP zones is determined by the presence of minute, yet adequate, W amount in the solid solution and a relatively low Al/(Al+Ti) ratio. This defines a compositional window not hitherto investigated.

## 2. Experimental and computational details

### 2.1. Synthesis

$\text{Ti}_{0.53}\text{Al}_{0.39}\text{W}_{0.08}\text{N}$  and  $\text{Ti}_{0.33}\text{Al}_{0.62}\text{W}_{0.05}\text{N}$  films are grown by hybrid W-HiPIMS/TiAl-DCMS co-sputtering method in an industrial CC800/9 magnetron sputtering system manufactured by CemeCon AG, Würselen, Germany. Si(001) substrates sequentially cleaned in acetone and isopropanol are mounted in the center of a sample holder facing the W target, with 21° angle between substrates and two DCMS targets (symmetrically placed on both sides of the W target) and at the 18 cm target-to-substrate distance. The base system pressure is 0.3 mPa ( $2.25 \times 10^{-6}$  Torr). The  $\text{N}_2$  and Ar flows are constant at 148 sccm and 360 sccm, so that the total gas pressure  $P_{\text{tot}}$  is 0.4 Pa. The power applied each TiAl target is 10 kW, while the W target operating in HiPIMS mode is powered to 2 kW (pulse length is 50  $\mu\text{s}$ , frequency = 200 Hz, and the peak target current density is  $\sim 0.80$  A/cm<sup>2</sup>). The negative substrate bias is applied synchronously with  $\text{W}^+$ -rich HiPIMS pulses [28] with the amplitude of 300 and 540 V for  $\text{Ti}_{0.53}\text{Al}_{0.39}\text{W}_{0.08}\text{N}$  and  $\text{Ti}_{0.33}\text{Al}_{0.62}\text{W}_{0.05}\text{N}$  films, respectively. These conditions were determined in our previous study to give dense films [29,30]. No external heating is used during film growth and the substrate temperature does not exceed  $\sim 140$  °C.

The reference  $\text{Ti}_{0.53}\text{Al}_{0.39}\text{W}_{0.08}\text{N}$  film with the same composition as one of the HiPIMS/DCMS films, in which GP zone formation is observed, is grown by DCMS process. This is to determine whether film composition or the ion irradiation conditions (mostly gas ions during DCMS vs. predominantly metal ions during HiPIMS/DCMS growth [25]) are decisive for the GP zones formation upon annealing. The reference  $\text{Ti}_{0.53}\text{Al}_{0.39}\text{W}_{0.08}\text{N}$  film is grown by DCMS process using the same set of targets. Powers applied to both TiAl targets are 10 kW (i.e., the same as

during the hybrid growth) while the average power on the W target now operating in DCMS mode is reduced to 520 W in order to maintain film composition. Such significant reduction in the W power (a factor of four) stems from the fact that during W-HiPIMS the significant fraction of the ionized W flux is attracted back to the target resulting in a 4-fold drop in the deposition rate [31,32]. The DCMS sample is grown at 470 °C and with a negative DC substrate bias of 60 V to achieve similar film density.

The annealing is done in vacuum (base pressure  $\sim 2.6 \times 10^{-3}$  Pa) with the heating rate of 10 °C/min to the annealing temperature  $T_a$ , which is in the range 500–1000 °C, and then kept at  $T_a$  for 2 h. The pressure during annealing varies in the range  $10^{-2}$  to  $10^{-3}$  Pa depending on  $T_a$ . Following anneal, the furnace is allowed to naturally cool down to room temperature.

### 2.2. Chemical, structural and mechanical characterization

Film compositions are determined by the time-of-flight elastic recoil detection analysis (ToF-ERDA).

An FEI Tecnai G2 TF 20 UT FEG microscope, operated at 200 kV is used to obtain an overview and high-resolution bright-field transmission electron microscopy (TEM) images as well as selected-area electron diffraction (SAED) patterns. Lattice- and atomic-resolved scanning transmission electron microscopy (STEM) imaging and energy-dispersive X-ray spectroscopy (EDX) mapping are carried out with double-C<sub>s</sub> corrected FEI Titan<sup>3</sup> 60–300, operated at 300 kV, equipped with the Super-X EDX system. The samples for TEM analysis were prepared by ion milling in a Gatan precision ion miller after fine mechanical polishing.

Nanoindentation hardness  $H$  is measured with an Ultra-Micro Indentation System nanoindenter performing 30 indents on each sample with a fixed load in the range of 17–20 mN using Berkovich diamond tip.

### 2.3. Ab initio calculations and molecular dynamics simulations

Density-functional theory (DFT) calculations and *ab initio* molecular dynamics (AIMD) simulations are carried out with the VASP code implemented with the projector augmented wave method [33,34]. The electronic exchange and correlation energies are modelled using the generalized gradient approximation of Perdew-Burke-Ernzerhof [35]. All DFT calculations employ  $\Gamma$ -point sampling of the reciprocal space and planewave cutoff energies of 400 eV. Total energies are calculated with accuracy of  $10^{-5}$  eV/supercell, relaxing supercell shape, volume, and atomic positions until forces on each atom are smaller than  $10^{-2}$  eV/Å.

Our supercell models have all exactly equal compositions  $\text{Ti}_{0.51}\text{Al}_{0.38}\text{W}_{0.08}\text{N}_{0.97}$ . They contain 3% vacancies on both sublattices because the parent  $\text{W}_x\text{N}_y$  is stabilized in a stoichiometric B1-like phase (NbO structure) by coexistence of cation and anion vacancies [36]. We employ supercells formed of 360 and 1440 B1-lattice sites to compare the energetics of random (Ti,Al,W)N solid solutions with that of tungsten GP precipitates of different sizes and shapes embedded in a (Ti,Al)N host matrix (denoted below as (Ti,Al)N+ $\text{W}_{\text{GP}}$ ). The supercells have [111]// $z$ , [1–10]// $x$ , and [11–2]// $y$  crystallographic relationship with the Cartesian axes. Given that the supercell vectors are *not* multiples of each other, a stochastic arrangement of metal and N species is sufficient to ensure low degree of short-range order. Small and large  $\text{W}_{\text{GP}}$  are modelled as disk-like agglomerates and ribbons disposed on a (111) lattice plane. Since B1  $\text{WN}_x$  phases are generally deficient in nitrogen, the anion vacancies in (Ti,Al)N+ $\text{W}_{\text{GP}}$  supercells are confined to (111) layers adjacent to the W cluster layer.

The thermodynamic stability of random (Ti,Al,W)N solid solutions and of (Ti,Al)N+ $\text{W}_{\text{GP}}$  is evaluated as a function of temperature via free energy calculations. We carry out total energy DFT calculations of random alloys and small W disks (360-sites supercells), large W disks and 1D periodic W ribbons with [110] and [112] edges (1440-sites

supercells). The calculations are repeated for different atomic arrangements of both fully disordered (Ti,Al,W)N and W-ordered (Ti,Al)N+W<sub>GP</sub> structures. Increasing the accuracy to  $2 \times 2 \times 2$  k-points reduces the energy per formula unit of W-ordered ( $-3.0$  meV/f.u.) and disordered ( $-2.4$  meV/f.u.) supercells. Thus,  $\Gamma$  sampling is considered sufficiently accurate to evaluate energy differences between ordered and disordered phases. The configurational entropy  $S_{\text{conf}}$  per formula unit is computed using the mean-field theory approximation. For (Ti,Al)N+W<sub>GP</sub> supercells, we omit the contribution of N vacancies and W atoms to  $S_{\text{conf}}$ . The vibrational entropy  $S_{\text{vib}}$  is assessed via direct AIMD simulations at 800 and 1300 K of the random (Ti,Al,W)N alloy with lowest total energy and for a small (Ti,Al)N+W<sub>GP</sub> structure. The simulations employ timestep integration of 1 fs. First, equilibrium volumes are determined via NPT sampling at 800 and 1300 K. Thus, the atomic trajectories are solved for 8.2 ps in the NVT ensemble coupled to the Nose-Hoover thermostat. The vibrational densities of states (from which we extract  $S_{\text{vib}}$ ) are obtained by Fourier transformation of the velocity-velocity autocorrelation function. The temperature-dependence of the free energy  $F$  (per formula unit) of competing phases is estimated as  $F(T) = E_{0K} - T[S_{\text{vib}}(T) + S_{\text{conf}}]$ , where  $E_{0K}$  is the total energy obtained by DFT calculations at 0 K. The vibrational free energy  $F_{\text{vib}} = -T \cdot S_{\text{vib}}$  of small (Ti,Al)N+W<sub>GP</sub> supercells at 800 and 1300 K remains approximately 10 meV/f.u. lower than  $F_{\text{vib}}$  of random alloys. Thus, we assume a constant  $\Delta F_{\text{vib}}$  difference between the free energies of random alloys and those of (Ti,Al)N+W<sub>GP</sub> structures at temperatures between 800 and 1300 K.

### 3. Results

ToF-ERDA reveals that the composition of Ti<sub>0.53</sub>Al<sub>0.39</sub>W<sub>0.08</sub>N and Ti<sub>0.33</sub>Al<sub>0.62</sub>W<sub>0.05</sub>N films remains constant during the annealing experiments within measurement accuracy.

Fig. 1 shows the nanoindentation hardness  $H$  as a function of the annealing temperature  $T_a$  for Ti<sub>0.53</sub>Al<sub>0.39</sub>W<sub>0.08</sub>N and Ti<sub>0.33</sub>Al<sub>0.62</sub>W<sub>0.05</sub>N films. The latter film shows the expected evolution [13]: the hardness reaches maximum of  $30.4 \pm 1.8$  GPa after annealing at 800 °C corresponding to the formation of the  $c$ -AlN phase. This is followed by a sharp decrease to  $25.7 \pm 1.7$  GPa with  $T_a = 950$  °C and  $19.5 \pm 1.6$  GPa with  $T_a = 1000$  °C ( $h$ -AlN detected, see below Fig. 2). In contrast, the as-deposited Ti<sub>0.53</sub>Al<sub>0.39</sub>W<sub>0.08</sub>N films exhibit a different behavior.  $H = 29.3 \pm 1.8$  GPa in as-deposited state and first decreases to  $26.7 \pm 1.9$  GPa after annealing at 500 °C, likely due to the relieve of the compressive stress (from  $-0.75 \pm 0.5$  GPa to  $0.03 \pm 0.03$  GPa) and defect annihilation, given that the growth temperature is very low ( $T_s < 140$  °C). With further  $T_a$  increase,  $H$  shows a continuous rise to the maximum of  $35.7 \pm 1.9$  GPa after annealing at 1000 °C. Markedly, even the formation of softer  $h$ -AlN phase (observed for  $T_a \geq 900$  °C, see Fig. 2) does not result in  $H$  decrease, in contrast to the Ti<sub>0.33</sub>Al<sub>0.62</sub>W<sub>0.05</sub>N films. This behavior is distinctly different to all previous studies of Ti-Al-N system reported in literature [13,15].

Fig. 2 presents cross-sectional bright-field overview TEM images and corresponding SAED patterns of the as-deposited and annealed films. The as-deposited Ti<sub>0.53</sub>Al<sub>0.39</sub>W<sub>0.08</sub>N film exhibits dense columnar microstructure (Fig. 2a). The SAED pattern of the film shows high intensity arc-like diffraction reflections matching B1-NaCl-structure phase with 111 fiber texture. The microstructural characterization of the film annealed at 800 °C does not show significant changes (see Supplementary Fig. S1) with respect to the as-deposited state (cf. Fig. 2a). The microstructure of the film does not change after the treatment at  $T_a = 900$  °C but a weak intensity  $h$ -AlN (10 $\bar{1}$ 0) ring reflection appears in SAED (Fig. 2b). After 2 h at  $T_a = 1000$  °C the intensity of the  $h$ -AlN (0001) reflections increases (Fig. 2c) and 20–30 nm size crystallites with bright contrast distributed along grain boundaries are visible in TEM image.

As-deposited Ti<sub>0.33</sub>Al<sub>0.62</sub>W<sub>0.05</sub>N films exhibit dense columnar microstructure, strong arc-like 111 and 002 diffraction spots

corresponding to B1-NaCl-structured phase similar to the one shown in Fig. 2a, b (see our previous study for details [30]). Ti<sub>0.33</sub>Al<sub>0.62</sub>W<sub>0.05</sub>N films after 2 h at 900 °C show dense microstructure with uniformly distributed 10–15 nm size crystallites with dark contrast (Fig. 2d). These crystallites appear in Z-contrast STEM image with bright contrast (Fig. 2d inset) which is indicative of high-density  $bcc$ -W phase. The film exhibits SAED pattern (Fig. 2d), which contains strong (10 $\bar{1}$ 0) reflections of the  $h$ -AlN phase and diffraction spots corresponding to the  $bcc$ -W phase. Note that the Ti<sub>0.53</sub>Al<sub>0.39</sub>W<sub>0.08</sub>N film annealed at 900 °C had no  $bcc$ -W phase and only weak  $h$ -AlN reflections (Fig. 2b).

It is evident that the significant hardness decrease of Ti<sub>0.33</sub>Al<sub>0.62</sub>W<sub>0.05</sub>N film after annealing at 900 °C is caused by the formation of soft  $h$ -AlN and, in addition, even softer  $bcc$ -W phase. Contrarily, although soft  $h$ -AlN is present in Ti<sub>0.53</sub>Al<sub>0.39</sub>W<sub>0.08</sub>N films after the 900 °C anneal, and its fraction increases after 2 h at 1000 °C, the hardness of that film continues to increase in the entire  $T_a$  range studied (cf. Fig. 1).

To understand the unexpected age-hardening behavior of Ti<sub>0.53</sub>Al<sub>0.39</sub>W<sub>0.08</sub>N films, the microstructure and local chemical composition is thoroughly characterized by means of high-resolution TEM (HRTEM), lattice- and atomically-resolved scanning TEM (STEM) imaging and energy-dispersive X-ray spectroscopy (EDX) mapping. An overview Z-contrast STEM image acquired from Ti<sub>0.53</sub>Al<sub>0.39</sub>W<sub>0.08</sub>N films annealed at 900 °C (Fig. 3a) reveals various regions in the film posing different contrasts. Distinctly lower average atomic number phase (dark contrast) can be observed forming at the boundary of cubic crystalline columnar grain while the inside of the grains exhibits mixed bright/dark contrast (discussed below). EDX mapping (Fig. 3b–e) of the area I in Fig. 3a provides evidence that the column boundary phase is Al-rich, while the column matrix contains homogeneously distributed W and non homogeneously distributed Ti and Al. The analysis of fast Fourier transforms (FFT) of the dark area (Fig. 3g) in the lattice-resolved STEM image (Fig. 3f) reveals reflections corresponding to B4-structured phase (Fig. 3g) implying that the Al-rich column boundary phase marked in Fig. 3a is the  $h$ -AlN phase, segregated at grain boundaries of the column matrix.

Whereas EDX mapping of the area II from within the column in Fig. 3a, (3i–l) reveals nanoscale domains enriched in Ti and Al, consistent with the STEM bright/dark contrast in Fig. 3a, with the modulation wavelength of the order of 3–7 nm, i.e., typical for spinodal decomposition of  $c$ -TiAlN, which has been shown to induce age hardening [13, 14]. W is homogeneously distributed in both Ti- and Al-rich domains (Figs. 3k and 4f below).

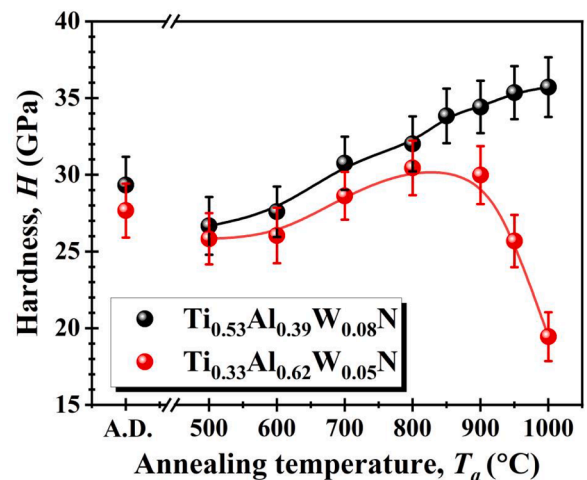
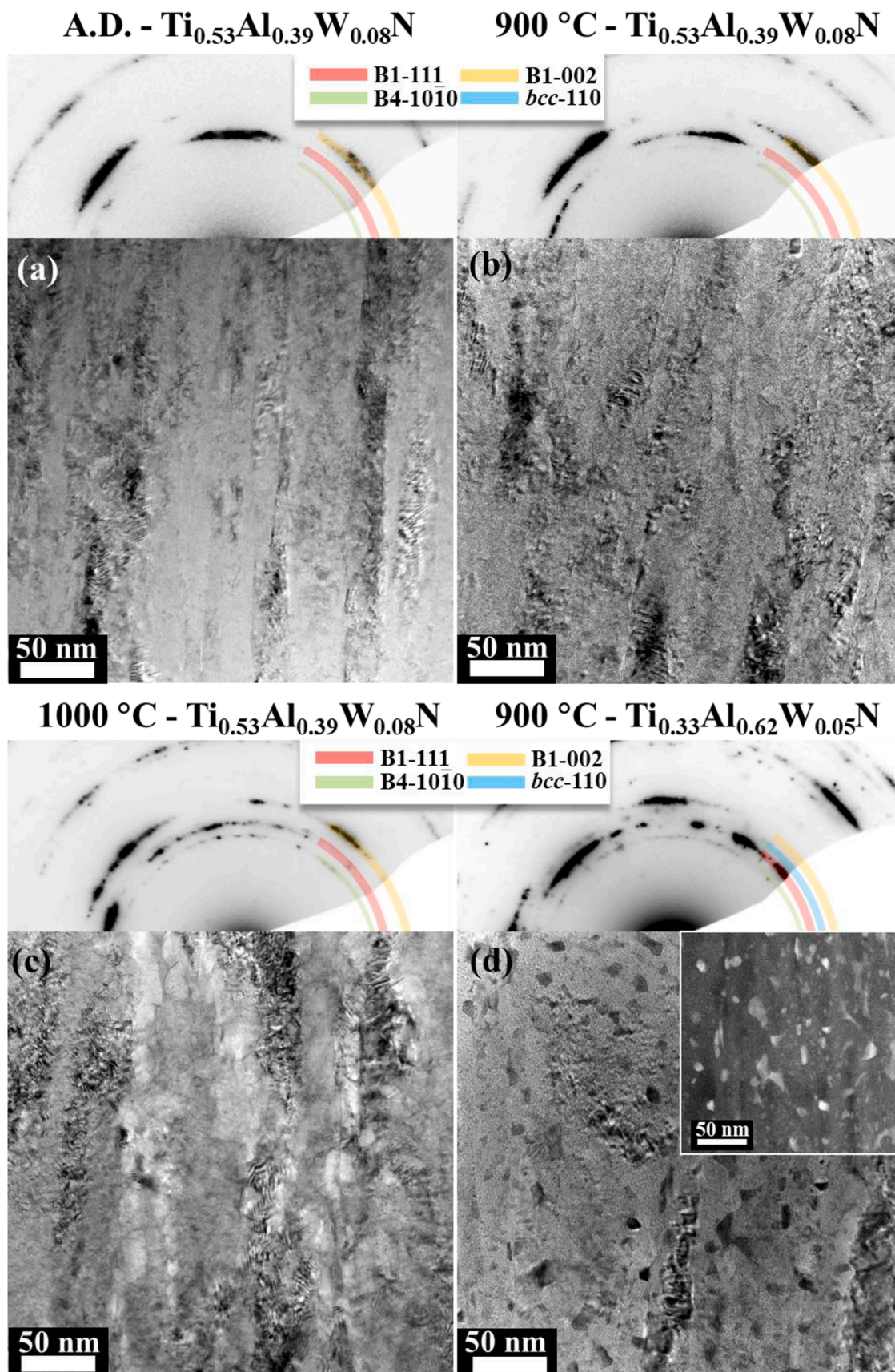


Fig. 1. Nanoindentation hardness  $H$  of Ti<sub>0.53</sub>Al<sub>0.39</sub>W<sub>0.08</sub>N and Ti<sub>0.33</sub>Al<sub>0.62</sub>W<sub>0.05</sub>N films as a function of annealing temperature ( $T_a$ ). Annealing is done in high vacuum for 2 h. As-deposited samples are denoted as “A.D.”.





**Fig. 2.** Cross-sectional bright-field overview TEM images and corresponding SAED patterns for as-deposited  $\text{Ti}_{0.53}\text{Al}_{0.39}\text{W}_{0.08}\text{N}$  films (a),  $\text{Ti}_{0.53}\text{Al}_{0.39}\text{W}_{0.08}\text{N}$  films annealed at 900 °C (b),  $\text{Ti}_{0.53}\text{Al}_{0.39}\text{W}_{0.08}\text{N}$  films annealed at 1000 °C (c), and  $\text{Ti}_{0.33}\text{Al}_{0.62}\text{W}_{0.05}\text{N}$  films annealed at 900 °C (d with inset showing Z-contrast STEM image). As-deposited samples are denoted as “A.D.”.



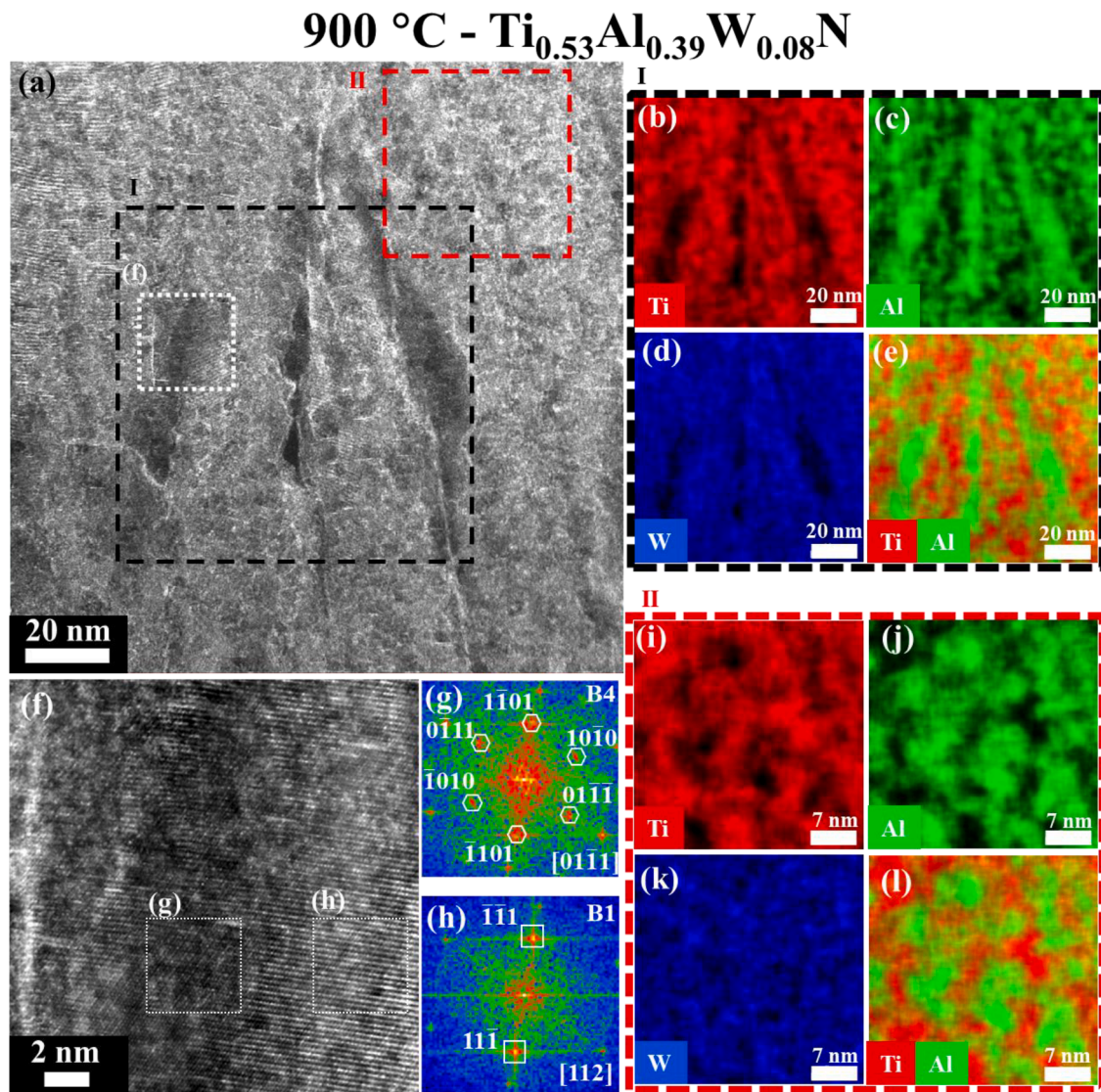


**Fig. 3.** Cross-sectional Z-contrast STEM images and EDX maps of  $\text{Ti}_{0.53}\text{Al}_{0.39}\text{W}_{0.08}\text{N}$  film after annealing at 900 °C. An overview STEM image from the  $150 \times 150 \text{ nm}^2$  area (a). EDX color-coded maps of three principal elements, that is, Ti (b), Al (c), W (d), and combined map of Ti-Al (e) acquired in the region I marked by the long-dashed black square in (a). Lattice-resolved STEM image of the region marked by the short-dashed white square in (a) showing  $h$ -AlN phase precipitation at grain boundaries (f) with FFT patterns of the dark (g, low Z) and bright (h, high Z) areas in (f) as indicated by white dot rectangles. EDX color-coded maps of three principal elements, that is, Ti (i), Al (j), W (k), and combined map of Ti-Al (l) acquired in the region II marked by the long-dashed red square in (a).

HRTEM images are taken from the column matrix of  $\text{Ti}_{0.53}\text{Al}_{0.39}\text{W}_{0.08}\text{N}$  film after annealing at 900 °C (Fig. 4a) and 1000 °C (Fig. 4b). The observations reveal atomic-layer-thick planar features of 2–3 nm in length viewed edge-on after annealing at 900 °C. Their average lengths increase to 3–5 nm after 2 h at  $T_a = 1000$  °C. The lattice-resolved STEM image from the column matrix of  $\text{Ti}_{0.53}\text{Al}_{0.39}\text{W}_{0.08}\text{N}$  film after annealing at 900 °C (Fig. 4c) viewed along the [110] zone axis together with corresponding FFT demonstrate clear lattice fringes corresponding to the metastable B1-NaCl structure of the column matrix which extend across bright and dark contrast regions consistent with spinodal-type decomposition on isostructural TiN- and AlN-rich domains. The bright planar features on individual 111 planes are homogeneously dispersed in the column matrix. Atomically-resolved STEM images (Fig. 4d) and EDX maps (Fig. 4e–h) from the individual features reveal that they are atomic-plane-thick W disks populating {111} planes of the cubic matrix. These atomic arrangements can be interpreted as GP (I) zones fully coherent with B1-NaCl-structured matrix [27]. GP(I) zones are originally known as atomic-plane-thick monoatomic Cu precipitates coherent with chemically distinct matrix phase and formed at

the early stage of age-hardening of Al based alloys [37,38].

To further understand the formation of GP(I) zones in  $\text{Ti}_{0.53}\text{Al}_{0.39}\text{W}_{0.08}\text{N}$  films, DFT calculations and AIMD simulations are employed. Fig. 5 shows the free energy of competing structures calculated as a function of temperature  $T$ . At 0 K (inset in top-left panel), the supercells of lowest energies containing small ( $\sim 1$  nm diameter) and large ( $\sim 2$  nm diameter) W disks are  $\sim 20$  and  $\sim 10$  meV/f.u., respectively, more stable than fully-disordered Ti-Al-W-N solid solutions. The supercells with a W ribbon with [110] edges exhibit the highest stability:  $\sim 30$  meV/atom lower than disordered solid solutions. Conversely, W ribbons with [112] edges (structure not shown) are predicted to be as stable as large W disks.

With increasing temperature, the configurational entropy contribution to the free energy increasingly favors lattice disorder. Note that the difference in vibrational free energies remains constant at  $\approx 10$  meV/f.u. for  $600 \leq T \leq 1500$  K, thus partially counterbalancing the configurational entropy effect. The free energy results shown in the figure indicate that nucleation of small (111) W disks surrounded by N-deficient (111) lattice planes is thermodynamically favored up to  $T = 1200 \pm 100$  K.



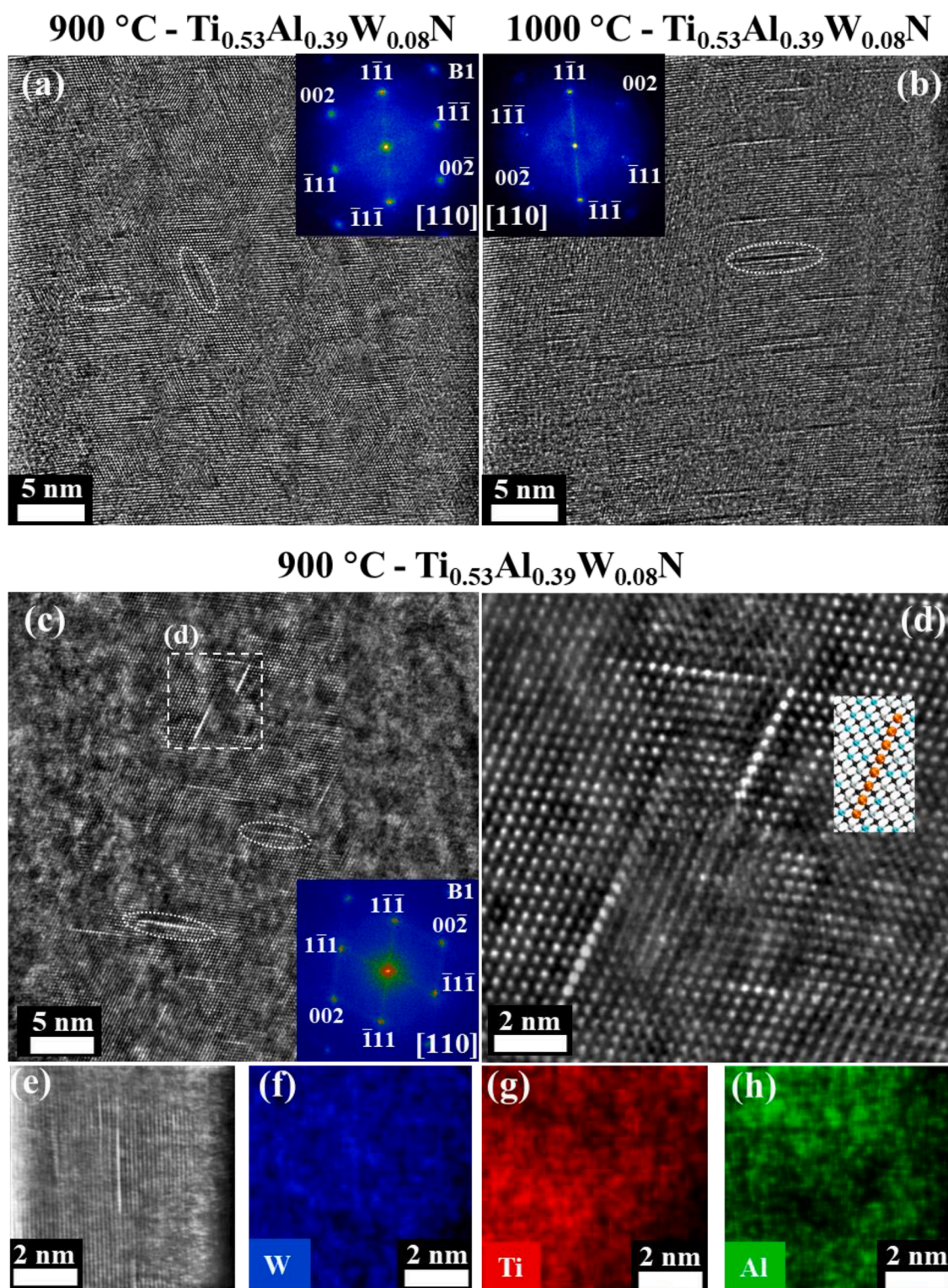


**Fig. 4.** Cross-sectional HRTEM images of  $\text{Ti}_{0.53}\text{Al}_{0.39}\text{W}_{0.08}\text{N}$  film after annealing at 900 °C (a) and 1000 °C (b) viewed along the [110] zone axis. Lattice-resolved Z-contrast STEM image taken along the [110] zone axis from B1-NaCl structure column matrix of  $\text{Ti}_{0.53}\text{Al}_{0.39}\text{W}_{0.08}\text{N}$  film after annealing at 900 °C (c) with corresponding FFT as an inset. Atomically-resolved STEM image (d) taken from the area marked by white-dash square in (c) with atomic structural model used in calculations as an inset (Color legend: black=N, silver=Ti, cyan=Al, orange=W). EDX color-coded maps of three principal elements, that is, W (f), Ti (g), Al (h), acquired in the region with GP (I) zone.

The results also suggest that, while growth of W precipitates to large disks is thermodynamically hindered, assembly of W atoms along  $\langle 110 \rangle$  lattice directions to form long W (111)-ribbons with [110] edges would be energetically favored up to  $1400 \pm 100$  K. Thus, the W-rich disks on 111-cation B1-NaCl sublattice can form via homogenous

nucleation and growth as incipient W-rich clusters, which form stochastically, capture diffusing W atoms. Lattice defects, such as vacancies on the nitrogen sublattice, could also serve as heterogenous nucleation sites.



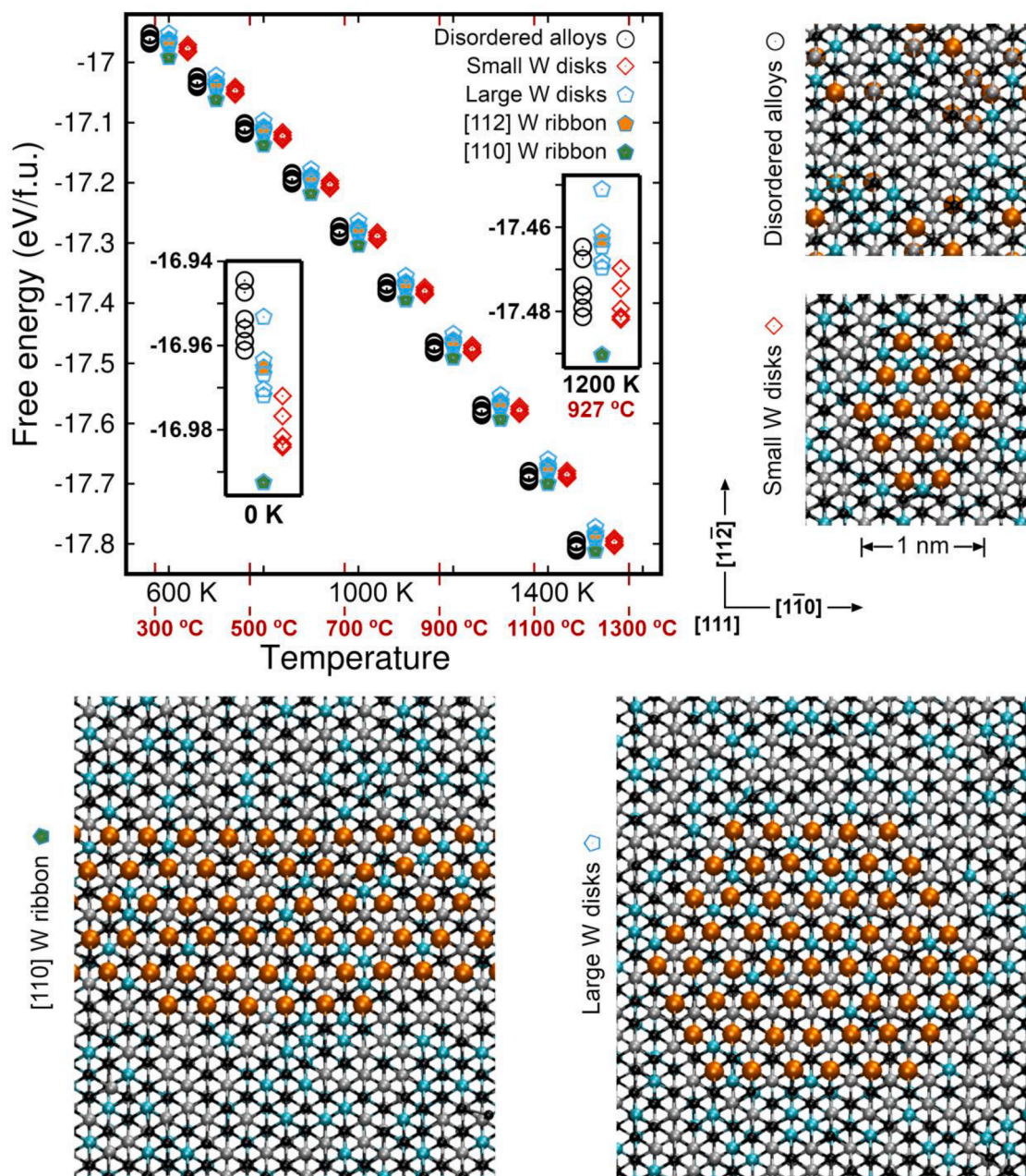


**Fig. 5.** DFT/AIMD free energies as a function of  $T$  of disordered (Ti,Al,W)N alloys as well as of small, large W disks, and 1D periodic W ribbons embedded in (Ti,Al)N disordered alloys. To facilitate readability, the energies of small (Ti,Al)N +  $W_{GP}$  structures and disordered alloys are offset in  $T$  by  $\pm 40$  K. The free-energy error bars are comparable to symbol sizes. Representative supercell structures are shown on the bottom and on the right. Color legend: black = N, silver = Ti, cyan = Al, orange = W.

#### 4. Discussion

The unexpected formation of GP(I) zones with W atoms populating  $\{111\}$  surface in annealed  $Ti_{0.53}Al_{0.39}W_{0.08}N$  films needs understanding. Both high-temperature annealed films,  $Ti_{0.33}Al_{0.62}W_{0.05}N$  and  $Ti_{0.53}Al_{0.39}W_{0.08}N$ , exhibit structural evolution that is in line with the well-known decomposition pathway in TiAlN system: supersaturated single-phase solid solution undergoes spinodal decomposition into  $c$ -TiN- and  $c$ -AlN-enriched nanodomains, and, upon overaging, subsequent local phase transformation of  $c$ -AlN into thermodynamically stable  $h$ -AlN takes place. Decomposition into cubic nanodomains is associated with initial age hardening in both films, whereas nucleation and growth of  $h$ -AlN resulting in a deterioration of mechanical properties is only observed in the  $Ti_{0.33}Al_{0.62}W_{0.05}N$  case.

A principal difference in structural evolution between the two films is the formation of GP(I) zones by W atoms populating  $\{111\}$  surface in the B1 matrix of  $Ti_{0.53}Al_{0.39}W_{0.08}N$  film and the precipitation of  $bcc$ -W in  $Ti_{0.33}Al_{0.62}W_{0.05}N$  layer, although W content in both films is similar. While both systems are metastable [39] (excluding possible impact of W) and the mixing enthalpy increases with  $x = Al/(Al+Ti)$ , the driving force for decomposition into thermodynamically stable phases is higher for the film with higher AlN content [2]. Therefore, the onset of decomposition into the stable phases occurs at lower  $T_a$  for the AlN-rich  $Ti_{0.33}Al_{0.62}W_{0.05}N$  film, in agreement with previous studies [15], which is evident as stronger  $h$ -AlN reflections in the SAED pattern shown in Fig. 2d (as compared to that from  $Ti_{0.53}Al_{0.39}W_{0.08}N$  film after annealing at 900 °C, Fig. 2b) [16,40]. Formation of  $h$ -AlN at relatively low  $T_a$  in the case of  $Ti_{0.33}Al_{0.62}W_{0.05}N$  films creates high-mobility diffusion pathways



along grain boundaries which enable precipitation of *bcc*-W grains.

In contrast, nucleation of the *h*-AlN phase within the grains is retarded in  $\text{Ti}_{0.53}\text{Al}_{0.39}\text{W}_{0.08}\text{N}$  films that together with low mobility of large W atoms in the B1 phase [41] results in diffusion of W leading to nucleation and growth of atomic layer precipitates on {111} planes, which can be interpreted as GP(I) zones.

Although *c*- $\text{Ti}_{1-z}\text{W}_z\text{N}$  solid solution was experimentally synthesized in a wide compositional range  $0 \leq z \leq 0.6$  [42], it is metastable with respect to the separate *c*-TiN and *h*- $\text{W}_2\text{N}$  phases [43]. Considering that *h*- $\text{W}_2\text{N}$  is among ground state phases of various W-N compounds [44] and the fact that cubic {111} surface follows a hexagonal pattern [45], {111} planes of the cubic matrix are preferential saddle sites for W atoms assembling towards known *h*- $\text{W}_2\text{N}$ . Ultimately, upon age hardening, W atom diffusion through the host cubic lattice results in local regions consisting of ordered W planes coherent with the matrix cubic lattice forming GP(I) zones. The bulk of the crystalline columnar grains remains cubic with compositionally modulated coherent *c*-Ti(W)N and Al(W)N-rich domains, and coherent GP(I) zones. DFT calculations show that GP(I) zones as small disks on {111} surface are thermodynamically favored up to 1200 K with a driving force to grow along [110] direction ultimately forming ribbons. Although GP(I) zones are observed in the matrix when viewed along [112] zone axis (see Supplementary Fig.S3), there is no evidence that they grow along [110]. Moreover, GP zone lengths along [110] do not change significantly upon the increase of annealing temperature from 900 to 1000 °C (c.f. Supplementary Fig. S3). However, the growth of W atoms into larger precipitates needs to compete with diffusion kinetics, recrystallization, defect annihilation, and concomitant phase transformations, such as spinodal decomposition. The latter, as seen in Fig. 3i-l, gives compositional fluctuations in the matrix, thus modifying the chemical environment that surrounds the GP zones. Since the composition of B1 {111} surface has significant effect on surface energetics and atomic diffusivity [45], GP zone growth direction can vary depending on the composition of a spinodally decomposed domain.

For full coherency, *c*-Ti(W)N and *c*-Al(W)N domains are strained by equal and opposite forces due to the small difference in lattice parameters. Moreover, GP(I) zones induce additional coherency strain fields in the matrix due to misfit between the GP zone and the matrix lattice [46]. The dark contrast on one side of GP(I) zones in the BF-TEM images originates from the strain field around the zones (Fig. 4a, b) [47]. The movement of dislocation is, thus, hindered because it is more difficult for dislocations to propagate through a strained material [48]. In addition, the long-range coherent composition modulation due to both cubic nano-domains and GP(I) zones results in spatially fluctuating elastic properties giving rise to Koehler type hardening [49,50]. The latter hardening mechanism is based on repelling shear stresses acting on dislocations gliding across the compositional gradient with difference in elastic shear modulus. Therefore, due to two sources of coherency strains and two sources of Koehler type hardening, i.e., coherent nano-domains of matrix phase and GP(I) zones, continuous age hardening of  $\text{Ti}_{0.53}\text{Al}_{0.39}\text{W}_{0.08}\text{N}$  films is observed even though precipitation of soft *h*-AlN takes place locally at grain boundaries. Since the precipitation of *h*-AlN and GP(I) zones starts in the same temperature range between 800 and 900 °C (cf. Fig. S1 and Fig. 2b, c), GP(I) zone hardening becomes active immediately when the softening mechanism due to *h*-AlN becomes operative. Moreover, GP(I) zone hardening not only compensates for softening due to *h*-AlN but also overcomes its adverse effect on hardness as the latter keeps increasing up to 1000 °C although the fraction of *h*-AlN increases (c.f. Figs. 1 and 2).

Considering the wealth of reports on TiAlN-based multielement nitrides films, one may ask the question why GP zone formation has not been reported before. While it might well have occurred in some studied system, GP zone formation has a very weak peak-broadening signature in XRD and may thus have gone unnoticed unless resolved by TEM as done here. A possible such case is from  $\text{Ti}_{1-x-y}\text{Al}_x\text{W}_y\text{N}$  coatings with  $x = 0.42$  and  $y = 0.05$ , see Figure 9 in [24]. Age hardening in TiAlN based

refractory nitride ceramics has also for decades since its discovery [13] been exclusively associated with the formation of coherent nanoscale domains via spinodal decomposition of a supersaturated solid solution exhibiting a clear XRD peak broadening and shoulder signature. The findings reported herein may stimulate revision of the age-hardening mechanisms in refractory nitride ceramics and allow to formulate general approaches required for synthesis of refractory ceramic with potential GP zone hardening ability. Towards that end, we note that alloying TiAlN with a wide range of group IVb and Vb transition metals (such as Zr [17], Hf [18], Ta [21,22] and Nb [19]) has thus shown to be an efficient way for a more pronounced age-hardening reflected in prolonged temperature window for age hardening or a higher hardness in comparison to TiAlN. The results presented here suggest that synthesis of ceramic nitride materials with potential to form GP zones can be realized by choosing a metastable-cubic solid-solution multielement system exhibiting a miscibility gap combined with a low affinity to nitrogen (as in the case of W) of a transition metal whose ground state nitride phase is other than *fcc*-NaCl. This expands possible choice of alloying transition metals to Ta, Mo, Re, Ru, and Os [51–53]. The strong sensitivity of GP zone formation to the Al content in the solid solution revealed in the present study also rationalizes why GP zones have not been reported in the previous studies on age-hardening of TiAlN based refractory nitride ceramics. With most attention spent on high-Al-content multielement nitrides with only minor additions of W, Ta, Mo, Hf, and Nb, the driving force for spinodal decomposition would greatly outnumber that of GP zone formation. The very GP formation and its expression would also be a function of the matrix registry, where an extensive spinodal process would render the lattice highly strained thus making {111} planes for a GP zone alignment less favorable or the features indistinguishable to the microscopist.

A possible concern is the effect of W addition on the oxidation of TiAlWN films under exploitation at ambient conditions, as it is known that WN tends to oxidize at 500–600 °C [54]. Because we use relatively small amount of W (4 at.%) embedded in oxidation resistant TiAlN, this effect will not likely interfere with the onset of GP zone hardening in the bulk of the coating. This topic, however, will require future experimental evaluation.

Importantly, GP(I) zones are also observed in  $\text{Ti}_{0.53}\text{Al}_{0.39}\text{W}_{0.08}\text{N}$  DCMS reference film (Supplementary Fig. S2) implying that GP(I) zone formation and associated hardening mechanism is a purely intrinsic property of the material system that obviously requires a solid solution initial state and does not depend on the synthesis method and related kinetic constraints. Instead, the Al and W concentrations are critical. Future experimental and theoretical studies are suggested for determining the chemical bimodal and spinodal for the components of the Ti-Al-W-N system. Temperature-time-transformation (TTT) diagrams will also help navigate between the different types and rates of transformations.

## 5. Conclusions

In summary, the results, we present here, demonstrate that age hardening of refractory nitride ceramics beyond the operation of spinodal decomposition is possible due to the activation of a novel for ceramic materials GP zone hardening. It is demonstrated by means of a set of complementary experimental and theoretical techniques that, upon annealing, supersaturated solid solution Ti-Al-W-N spinodally decomposes into Ti(W)N-rich and Al(W)N-rich nanodomains with {111} planes populated by atomic-plane-thick W in the form of GP(I) zones. This GP zone formation represents an additional source of coherency strain for Koehler stress that hinders dislocation motion, thus increasing hardness and effectively counteracting softening from *h*-AlN precipitation. A broader potential impact of this work is that the hardening mechanism presented here can be put to work in other ceramic systems, widening the materials design and operational window for production of advanced ceramics.

## Declaration of Competing Interest

The authors declare that they have no known competing financial interests or personal relationships that could have appeared to influence the work reported in this paper.

## Acknowledgments

The authors acknowledge the financial support of the Swedish Research Council VR Grant 2018-03957, 2021-03652 and 2021-04426, the Swedish Energy Agency under project 51201-1, the Åforsk Foundation Grant 22-4, the Knut and Alice Wallenberg Foundation Scholar Grants KAW2016.0358 and KAW2019.0290, the Carl Tryggers Stiftelse contract CTS 20:150 and 21:1272, and the Competence Center Functional Nanoscale Materials (FunMat-II) VINNOVA grant 2022-03071. Support from the Swedish Research Council VR-RFI (2017-00646\_9) for the Accelerator based ion-technological center and from the Swedish Foundation for Strategic Research (contract RIF14-0053) for the Tandem Accelerator Laboratory in Uppsala University is acknowledged. Swedish Research Council and SSF for access to ARTEMI, the Swedish National Infrastructure in Advanced Electron Microscopy (2021-00171 and RIF21-0026). All simulations were carried out using the resources provided by the Swedish National Infrastructure for Computing (SNIC) – partially funded by the Swedish Research Council through Grant Agreement No VR-2018-0597.

## Supplementary materials

Supplementary material associated with this article can be found, in the online version, at [doi:10.1016/j.actamat.2023.119105](https://doi.org/10.1016/j.actamat.2023.119105).

## References

- [1] A. Hörling, L. Hultman, M. Odén, J. Sjölen, L. Karlsson, Thermal stability of arc evaporated high aluminum-content Ti<sub>1-x</sub>Al<sub>x</sub>N thin films, *J. Vac. Sci. Technol. A Vacuum Surf. Film* 20 (2002) 1815, <https://doi.org/10.1116/1.1503784>.
- [2] P.H. Mayrhofer, D. Music, J.M. Schneider, Ab initio calculated binodal and spinodal of cubic Ti<sub>1-x</sub>Al<sub>x</sub>N, *Appl. Phys. Lett.* 88 (2006) 10–13, <https://doi.org/10.1063/1.2177630>.
- [3] O. Knotek, On structure and properties of sputtered Ti and Al based hard compound films, *J. Vac. Sci. Technol. A Vacuum Surf. Film* 4 (1986) 2695, <https://doi.org/10.1116/1.573708>.
- [4] W.D. Münz, Titanium aluminum nitride films: a new alternative to TiN coatings, *J. Vac. Sci. Technol. A Vacuum Surf. Film* 4 (1986) 2717, <https://doi.org/10.1116/1.573713>.
- [5] G. Greczynski, L. Hultman, M. Odén, X-ray photoelectron spectroscopy studies of Ti<sub>1-x</sub>Al<sub>x</sub>N (0 ≤ x ≤ 0.83) high-temperature oxidation: the crucial role of Al concentration, *Surf. Coat. Technol.* 374 (2019) 923–934, <https://doi.org/10.1016/j.surfcoat.2019.06.081>.
- [6] N. Shulumba, O. Hellman, Z. Raza, B. Alling, J. Barrirero, F. Mücklich, I. A. Abrikosov, M. Odén, Lattice vibrations change the solid solubility of an alloy at high temperatures, *Phys. Rev. Lett.* 117 (2016) 1–6, <https://doi.org/10.1103/PhysRevLett.117.205502>.
- [7] G. Hakansson, T.F. Group, D. McIntyre, J.E. Greene, Microstructure and physical properties of polycrystalline metastable Ti<sub>0.5</sub>Al<sub>0.5</sub>N alloys grown by d.c. magnetron sputter deposition, *Thin. Solid Films* 153 (1987) 55–65, [https://doi.org/10.1016/0040-6090\(87\)90169-6](https://doi.org/10.1016/0040-6090(87)90169-6).
- [8] J.M. Andersson, J. Vetter, J. Müller, J. Sjölen, Structural effects of energy input during growth of Ti<sub>1-x</sub>Al<sub>x</sub>N (0.55 ≤ x ≤ 0.66) coatings by cathodic arc evaporation, *Surf. Coat. Technol.* 240 (2014) 211–220, <https://doi.org/10.1016/j.surfcoat.2013.12.018>.
- [9] G. Greczynski, J. Lu, M. Johansson, J. Jensen, I. Petrov, J.E. Greene, L. Hultman, Selection of metal ion irradiation for controlling Ti<sub>1-x</sub>Al<sub>x</sub>N alloy growth via hybrid HIPIMS/magnetron co-sputtering, *Vacuum* 86 (2012) 1036–1040, <https://doi.org/10.1016/j.vacuum.2011.10.027>.
- [10] L.A. Donohue, I.J. Smith, W.D. Münz, I. Petrov, J.E. Greene, Microstructure and oxidation-resistance of Ti<sub>1-x</sub>Al<sub>x</sub>N layers grown by combined steered-arc/unbalanced-magnetron-sputter deposition, *Surf. Coat. Technol.* 94–95 (1997) 226–231, [https://doi.org/10.1016/S0257-8972\(97\)00249-1](https://doi.org/10.1016/S0257-8972(97)00249-1).
- [11] G. Greczynski, J. Lu, M.P. Johansson, J. Jensen, I. Petrov, J.E. Greene, L. Hultman, Role of Ti<sup>+</sup> and Al<sup>n+</sup> ion irradiation (n=1, 2) during Ti<sub>1-x</sub>Al<sub>x</sub>N alloy film growth in a hybrid HIPIMS/magnetron mode, *Surf. Coat. Technol.* 206 (2012) 4202–4211, <https://doi.org/10.1016/j.surfcoat.2012.04.024>.
- [12] A. Knutsson, M.P. Johansson, P.O. Persson, L. Hultman, M. Odén, Thermal decomposition products in arc evaporated TiAlN/TiN multilayers, *Appl. Phys. Lett.* 93 (2008), <https://doi.org/10.1063/1.2998588>.
- [13] P.H. Mayrhofer, A. Hörling, L. Karlsson, J. Sjölen, T. Larsson, C. Mitterer, L. Hultman, Self-organized nanostructures in the Ti–Al–N system, *Appl. Phys. Lett.* 83 (2003) 2049–2051, <https://doi.org/10.1063/1.1608464>.
- [14] M.P. Johansson Jösaar, N. Norrby, J. Ullbrand, R. M'Saoubi, M. Odén, Anisotropy effects on microstructure and properties in decomposed arc evaporated Ti<sub>1-x</sub>Al<sub>x</sub>N coatings during metal cutting, *Surf. Coat. Technol.* 235 (2013) 181–185, <https://doi.org/10.1016/j.surfcoat.2013.07.031>.
- [15] N. Norrby, L. Rogström, M.P. Johansson-Jösaar, N. Schell, M. Odén, *In situ* X-ray scattering study of the cubic to hexagonal transformation of AlN in Ti<sub>1-x</sub>Al<sub>x</sub>N, *Acta Mater.* 73 (2014) 205–214, <https://doi.org/10.1016/j.actamat.2014.04.014>.
- [16] L. Chen, J. Paulitsch, Y. Du, P.H. Mayrhofer, Thermal stability and oxidation resistance of Ti–Al–N coatings, *Surf. Coat. Technol.* 206 (2012) 2954–2960, <https://doi.org/10.1016/j.surfcoat.2011.12.028>.
- [17] L. Chen, D. Holec, Y. Du, P.H. Mayrhofer, Influence of Zr on structure, mechanical and thermal properties of Ti–Al–N, *Thin. Solid Films* 519 (2011) 5503–5510, <https://doi.org/10.1016/j.tsf.2011.03.139>.
- [18] R. Rachbauer, A. Blutmager, D. Holec, P.H. Mayrhofer, Effect of Hf on structure and age hardening of Ti–Al–N thin films, *Surf. Coat. Technol.* 206 (2012) 2667–2672, <https://doi.org/10.1016/j.surfcoat.2011.11.020>.
- [19] Y.H. Chen, J.J. Roa, C.H. Yu, M.P. Johansson-Jösaar, J.M. Andersson, M. J. Anglada, M. Odén, L. Rogström, Enhanced thermal stability and fracture toughness of TiAlN coatings by Cr, Nb and V-alloying, *Surf. Coat. Technol.* 342 (2018) 85–93, <https://doi.org/10.1016/j.surfcoat.2018.02.059>.
- [20] S.A. Glatz, V. Moraes, C.M. Koller, H. Riedl, H. Bolvardi, S. Kolozsvári, P. H. Mayrhofer, Effect of Mo on the thermal stability, oxidation resistance, and tribo-mechanical properties of arc evaporated Ti–Al–N coatings, *J. Vac. Sci. Technol. A* 35 (2017) 61515, <https://doi.org/10.1116/1.5009743>.
- [21] W.M. Seidl, M. Bartosik, S. Kolozsvári, H. Bolvardi, P.H. Mayrhofer, Improved mechanical properties, thermal stabilities, and oxidation resistance of arc evaporated Ti–Al–N coatings through alloying with Ta, *Surf. Coat. Technol.* 344 (2018) 244–249, <https://doi.org/10.1016/j.surfcoat.2018.03.014>.
- [22] R. Rachbauer, D. Holec, P.H. Mayrhofer, Increased thermal stability of Ti–Al–N thin films by Ta alloying, *Surf. Coat. Technol.* 211 (2012) 98–103, <https://doi.org/10.1016/j.surfcoat.2011.07.009>.
- [23] T. Reeswinkel, D.G. Sangiovanni, V. Chirita, L. Hultman, J.M. Schneider, Structure and mechanical properties of TiAlN–WN<sub>x</sub> thin films, *Surf. Coat. Technol.* 205 (2011) 4821–4827, <https://doi.org/10.1016/j.surfcoat.2011.04.066>.
- [24] S.A. Glatz, H. Bolvardi, S. Kolozsvári, C.M. Koller, H. Riedl, P.H. Mayrhofer, Arc evaporated W-alloyed Ti–Al–N coatings for improved thermal stability, mechanical, and tribological properties, *Surf. Coat. Technol.* 332 (2017) 275–282, <https://doi.org/10.1016/j.surfcoat.2017.05.097>.
- [25] G. Greczynski, I. Petrov, J.E. Greene, L. Hultman, Paradigm shift in thin-film growth by magnetron sputtering : from gas-ion to metal-ion irradiation of the growing film, *J. Vac. Sci. Technol. A* 37 (2019), 060801, <https://doi.org/10.1116/1.5121226>.
- [26] G. Greczynski, J. Lu, S. Bolz, W. Kölker, C. Schiffrers, O. Lemmer, I. Petrov, J. E. Greene, L. Hultman, Novel strategy for low-temperature, high-rate growth of dense, hard, and stress-free refractory ceramic thin films, *J. Vac. Sci. Technol. A Vacuum Surf. Film* 32 (2014), 041515, <https://doi.org/10.1116/1.4884575>.
- [27] F.W. Gayle, M. Goodway, Precipitation hardening in the first aerospace aluminum alloy: the Wright Flyer crankcase, *Science* 266 (80) (1994) 1015–1017.
- [28] G. Greczynski, J. Lu, J. Jensen, I. Petrov, J.E. Greene, S. Bolz, W. Kölker, C. Schiffrers, O. Lemmer, L. Hultman, Metal versus rare-gas ion irradiation during Ti<sub>1-x</sub>Al<sub>x</sub>N film growth by hybrid high power pulsed magnetron/dc magnetron co-sputtering using synchronized pulsed substrate bias, *J. Vac. Sci. Technol. A Vacuum Surf. Film* 30 (2012), 061504, <https://doi.org/10.1116/1.4750485>.
- [29] X. Li, B. Bakhit, M.P. Johansson Jösaar, I. Petrov, L. Hultman, G. Greczynski, Towards energy-efficient physical vapor deposition: mapping out the effects of W+ energy and concentration on the densification of TiAlWN thin films grown with no external heating, *Surf. Coat. Technol.* 424 (2021), 127639, <https://doi.org/10.1016/j.surfcoat.2021.127639>.
- [30] X. Li, B. Bakhit, M.P. Johansson Jösaar, I. Petrov, L. Hultman, G. Greczynski, Dense, single-phase, hard, and stress-free Ti<sub>0.32</sub>Al<sub>0.63</sub>W<sub>0.05</sub>N films grown by magnetron sputtering with dramatically reduced energy consumption, *Sci. Rep.* 12 (2022) 1–10, <https://doi.org/10.1038/s41598-022-05975-5>.
- [31] G. Greczynski, L. Hultman, Peak amplitude of target current determines deposition rate loss during high power pulsed magnetron sputtering, *Vacuum* 124 (2016) 1–4, <https://doi.org/10.1016/j.vacuum.2015.11.004>.
- [32] D.J. Christie, Target material pathways model for high power pulsed magnetron sputtering, *J. Vac. Sci. Technol. A Vacuum Surf. Film* 23 (2005) 330–335, <https://doi.org/10.1116/1.1865133>.
- [33] G. Kresse, J. Furthmüller, Efficiency of ab-initio total energy calculations for metals and semiconductors using a plane-wave basis set, *Comput. Mater. Sci.* 6 (1996) 15–50, [https://doi.org/10.1016/0927-0256\(96\)00008-0](https://doi.org/10.1016/0927-0256(96)00008-0).
- [34] D. Joubert, From ultrasoft pseudopotentials to the projector augmented-wave method, *Phys. Rev. B Condens. Matter Mater. Phys.* 59 (1999) 1758–1775, <https://doi.org/10.1103/PhysRevB.59.1758>.
- [35] J.P. Perdew, K. Burke, M. Ernzerhof, Generalized gradient approximation made simple, *Phys. Rev. Lett.* 77 (1996) 3865–3868, <https://doi.org/10.1103/PhysRevLett.77.3865>.
- [36] B.D. Ozsdolay, C.P. Mulligan, K. Balasubramanian, L. Huang, S.V. Khare, D. Gall, Cubic β-WN<sub>x</sub> layers: growth and properties vs N-to-W ratio, *Surf. Coat. Technol.* 304 (2016) 98–107, <https://doi.org/10.1016/j.surfcoat.2016.06.079>.

- [37] S.J. Andersen, C.D. Marioara, J. Friis, S. Wenner, R. Holmestad, Precipitates in aluminium alloys, *Adv. Phys.* **X** 3 (2018) 790–814, <https://doi.org/10.1080/23746149.2018.1479984>.
- [38] A. Guinier, Structure of age-hardened aluminium-copper alloys, *Nature* **142** (1938) 569–570, <https://doi.org/10.1038/142569b0>.
- [39] P.H. Mayrhofer, L. Hultman, J.M. Schneider, P. Staron, H. Clemens, Spinodal decomposition of cubic Ti 1 – x Al x N : comparison between experiments and modeling, *Int. J. Mat. Res.* **2** (2007).
- [40] J. Zhou, J. Zhong, L. Chen, L. Zhang, Y. Du, Z.K. Liu, P.H. Mayrhofer, Phase equilibria, thermodynamics and microstructure simulation of metastable spinodal decomposition in c-Ti1 – xAlxN coatings, *Calphad* **56** (2017) 92–101, <https://doi.org/10.1016/j.calphad.2016.12.006>.
- [41] L. Hultman, Thermal stability of nitride thin films, *Vacuum* **57** (2000) 1–30, [https://doi.org/10.1016/S0042-207X\(00\)00143-3](https://doi.org/10.1016/S0042-207X(00)00143-3).
- [42] F. Tian, J. D'Arcy-Gall, T.Y. Lee, M. Sardela, D. Gall, I. Petrov, J.E. Greene, Epitaxial Ti1-xWxN alloys grown on MgO(001) by ultrahigh vacuum reactive magnetron sputtering: electronic properties and long-range cation ordering, *J. Vac. Sci. Technol. A Vacuum Surf. Film* **21** (2003) 140–146, <https://doi.org/10.1116/1.1525818>.
- [43] D. Edström, D.G. Sangiovanni, L. Hultman, V. Chirita, Effects of atomic ordering on the elastic properties of TiN- and VN-based ternary alloys, *Thin. Solid Films* **571** (2014) 145–153, <https://doi.org/10.1016/j.tsf.2014.09.048>.
- [44] M.J. Mehl, D. Finkenstadt, C. Dane, G.L.W. Hart, S. Curtarolo, Finding the stable structures of N1-xWx with an ab initio high-throughput approach, *Phys. Rev. B Condens. Matter Mater. Phys.* **91** (2015) 1–19, <https://doi.org/10.1103/PhysRevB.91.184110>.
- [45] C. Tholander, B. Alling, F. Tasnadi, J.E. Greene, L. Hultman, Effect of Al substitution on Ti, Al, and N adatom dynamics on TiN(001), (011), and (111) surfaces, *Surf. Sci.* **630** (2014) 28–40, <https://doi.org/10.1016/j.susc.2014.06.010>.
- [46] C.V. Singh, D.H. Warner, Mechanisms of Guinier-Preston zone hardening in the athermal limit, *Acta Mater.* **58** (2010) 5797–5805, <https://doi.org/10.1016/j.actamat.2010.06.055>.
- [47] R.B. Nicholson, J. Nutting, Direct observation of the strain field produced by coherent precipitated particles in an age-hardened alloy, *Philos. Mag.* **3** (1958) 531–535, <https://doi.org/10.1080/14786435808244578>.
- [48] J. Cahn, Hardening by spinodal decomposition, *Acta Metall.* **11** (1963) 1275–1282, [https://doi.org/10.1016/0001-6160\(63\)90022-1](https://doi.org/10.1016/0001-6160(63)90022-1).
- [49] J.S. Koehler, Attempt to design a strong solid, *Phys. Rev. B.* **2** (1968) 547–551, <https://doi.org/10.1103/PhysRevB.2.547>.
- [50] F. Tasnádi, I.A. Abrikosov, L. Rogström, J. Almer, M.P. Johansson, M. Oden, Significant elastic anisotropy in Ti1-x Alx N alloys, *Appl. Phys. Lett.* **97** (2010) 23–26, <https://doi.org/10.1063/1.3524502>.
- [51] Y. Zhang, L. Wu, B. Wan, Y. Lin, Q. Hu, Y. Zhao, R. Gao, Z. Li, J. Zhang, H. Gou, Diverse ruthenium nitrides stabilized under pressure: a theoretical prediction, *Sci. Rep.* **6** (2016) 1–9, <https://doi.org/10.1038/srep33506>.
- [52] C. Zang, H. Sun, J.S. Tse, C. Chen, Indentation strength of ultraincompressible rhenium boride, carbide, and nitride from first-principles calculations, *Phys. Rev. B Condens. Matter Mater. Phys.* **86** (2012) 1–9, <https://doi.org/10.1103/PhysRevB.86.014108>.
- [53] A. Friedrich, B. Winkler, L. Bayarjargal, W. Morgenroth, E.A. Juarez-Arellano, V. Milman, K. Refson, M. Kunz, K. Chen, Novel rhenium nitrides, *Phys. Rev. Lett.* **105** (2010) 1–4, <https://doi.org/10.1103/PhysRevLett.105.085504>.
- [54] G. Gassner, P.H. Mayrhofer, K. Kutschej, C. Mitterer, M. Kathrein, Magnéli phase formation of PVD Mo-N and W-N coatings, *Surf. Coat. Technol.* **201** (2006) 3335–3341, <https://doi.org/10.1016/j.surfcoat.2006.07.067>.